Effects of electron-phonon coupling on absorption spectrum: *K* edge of hexagonal boron nitride

Ferenc Karsai and Moritz Humer
Department of Physics, University of Vienna, Sensengasse 8, Vienna 1090, Austria

Espen Flage-Larsen
SINTEF Materials and Chemistry, Oslo 7465, Norway

Peter Blaha
Institute of Materials Chemistry, Vienna University of Technology, Getreidemarkt 9/165-TC, Vienna 1060, Austria

Georg Kresse
Department of Physics, University of Vienna, Sensengasse 8, Vienna 1090, Austria

(Received 11 October 2018; published 26 December 2018)

A detailed analysis of the theoretical x-ray absorption near-edge structures (XANES) for the boron and nitrogen K edge in hexagonal boron nitride (h-BN) employing density-functional theory calculations is presented. The supercell core-hole method and the Bethe-Salpeter equation are used for the description of electron-hole interactions. The calculations are carried out with two different codes, the VASP and the WIEN2K codes, employing the projector augmented-wave and the full-potential linear augmented-plane-wave methods, respectively. We find close agreement between spectra obtained from the two codes and between calculations using the supercell core-hole method and the Bethe-Salpeter approach. All our calculations, as well as previous calculations using the ground-state structure, yield a single $2p_{\sigma^*}$ peak in the boron K-edge spectrum and hence fail to describe the experimental double-peak structure. We find that the inclusion of electron-phonon interactions is crucial to obtain the experimentally observed double-peak structure. We include these effects fully parameter free and *ab initio* using a one-shot sampling method and obtain excellent agreement with experiment.

DOI: 10.1103/PhysRevB.98.235205

I. INTRODUCTION

Hexagonal boron nitride (h-BN) has a similar structure as graphite with alternating atoms in the hexagonal plane and with a stacking sequence such that boron and nitrogen atoms are on top of each other out of plane. It is considered in a growing number of applications due to its high thermal stability and similarity to graphite, for instance, in deep ultraviolet light emitters [1] and as a supporting substrate for graphene [2]. A thorough knowledge of its electronic, chemical, and structural properties is crucial to be able to optimally exploit the unique properties of h-BN. One very powerful experimental method for characterization of h-BN is x-ray absorption near-edge spectroscopy (XANES). This method excites boron and nitrogen 1s electrons mainly into the corresponding unoccupied p states. In order to understand and interpret the experimental spectra, theoretical investigations are indispensable and provide a deeper understanding of the detailed excitation process.

Several experimental XANES spectra of h-BN were published [3–10], but also high-resolution electron energy-loss (EELS) spectra have been reported [11] and agree very well with the corresponding XANES spectra. Due to the strong localization of core states, large electron-hole interactions are present in the K-edge spectrum of both boron [8] and nitrogen [12–15]. For boron, the main transitions of the K edges were shown to originate from the excitation of the boron 1s core state into antibonding $2p_{\pi^*}$ states forming a sharp exciton with a very long lifetime [8] and subsequently into $2p_{\sigma^*}$ states, which form broader features. The first peak is well reproduced in all theoretical calculations, but all previous theoretical studies failed to reproduce the shape of the second peak. For nitrogen, the main transitions of the K edge are also due to excitation of the nitrogen 1s core state into antibonding $2p_{\pi^*}$ and subsequent $2p_{\sigma^*}$ states. However, compared to boron, the peaks are much broader, and the $2p_{\pi^*}$ peak shows a slowly decaying right shoulder. All previous calculations failed to describe this shoulder and underestimate the energy separation between $2p_{\pi^*}$ and $2p_{\sigma^*}$ states.

Obviously in the case of strong electron-hole interactions, one cannot use the ground-state electronic structure as obtained from a density-functional theory (DFT) calculation, but one must explicitly incorporate electron-hole interactions in the calculation of the theoretical spectra. One option is to represent the solid with a supercell using periodic boundary conditions (or a sizable finite cluster [16]) and create a core hole by removing a core electron and placing it into the conduction bands [17–19]. In this way, the screening of the electron and hole are automatically incorporated in the calculations. We will refer to this method as the supercell core-hole (SCH) method throughout this work. The transition matrix elements between core and conduction band states are usually calculated in the dipole approximation and hence can be used for all spectroscopic methods that are probing electric dipole transitions of core electrons (see Ref. [20] for the calculation

of energy-loss near-edge spectra using the SCH method). Another method to describe excitonic effects is the inclusion of electron-hole effects by solving the Bethe-Salpeter equation [21–24] (BSE) on top of the ground-state electronic structure calculations [25,26]. Unfortunately, this method is very time consuming, but due to the steadily growing compute power, BSE calculations are becoming routine fairly rapidly. This is in particular true for the description of optical spectroscopy in the UV and visible light range [27,28], with several BSE calculations appearing recently for bulk and single layers of *h*-BN [29,30]. Furthermore, few publications on different materials employing the BSE for the calculation of x-ray absorption spectra have been published [26,31–36]. Already in 1998 and 1999, boron *K* edges and resonant inelastic x-ray scattering (RIXS) calculations using the BSE were reported [37–40], although these early calculations might not have been fully converged with respect to the computational parameters.

In literature, there are numerous calculations for *h*-BN employing the SCH method [11,13,41–43]. At first glance, they all obtain similar results and agreement with experiment is generally reasonable but not perfect. The first peak of the experimental boron *K*-edge spectrum is well reproduced in all calculations. However, all previous theoretical studies fail to reproduce the second, the $2p_{\sigma^*}$ peak: experiments show a double peak at 199 eV, whereas theory predicts a single peak. In the majority of the previously published studies, the discussion of this discrepancy is omitted. Only few publications speculate about the origin of the double peak. For instance, Ref. [44] suggests that vacancies or defects in the crystal could cause a splitting of the $2p_{\sigma^*}$ peak. We think that this is not a convincing explanation since very high vacancy concentrations would be required to yield a double peak with equal height for each of its subpeaks. Furthermore, the double-peak structure is also retained in experiments using only very few layers [10], where the defect concentration is usually small. We rather think that lattice displacements due to electron-phonon couplings are the main reason for the formation of the double peak. In a recent publication [45] it was demonstrated on the example of several light-element compounds that thermal vibrations can have noticeable effects on XANES and NMR spectra. Furthermore, in a recent synchrotron measurement [8] it was shown that a very small splitting of approximately 0.1 eV is observed for the first peak of the boron *K*-edge spectrum. The authors claim that the splitting is most probably driven by exciton-phonon interactions. Motivated by this result we decided to incorporate the effects of vibrational displacements in our calculations and study their effect on the core-hole spectra.

In this work, we reexamine the *K*-edge spectra in *h*-BN in great detail. We employ the SCH and BSE approach and carefully investigate the differences between both methods. To the best of our knowledge, no publication exists employing the full Bethe-Salpeter equation to both, XANES boron and nitrogen *K* edges in *h*-BN. However, the crucial improvement of our work over previous studies is the inclusion of EPC in the SCH calculations via statistical sampling methods.

The structure of this paper is as follows. First, an outline of the theory is given in Secs. II, III, and IV. This is followed by a description of the computational methods and parameters in Sec. V. In Sec. VI, the boron and nitrogen *K*-edge spectra are investigated using different methods and codes. The examinations are first performed at the ground-state structure. The inclusion of vibrational displacements on the spectra is examined in Sec. VII. In this section, we also carefully examine the origin of the double-peak structure of the boron $2p_{\sigma^*}$ peak. We finally conclude the paper in Sec. VIII.

II. DIELECTRIC FUNCTION FOR CORE ELECTRONS

Since the wavelength of the electromagnetic waves in absorption spectroscopy is usually much larger than the characteristic momentum in solids, we start from the transversal expression for the imaginary part of the dielectric function in the long-wavelength limit ($\mathbf{q} = 0$) which is directly proportional to the absorption spectrum

$$\epsilon^{(2)}_{\alpha\beta}(\omega, \mathbf{q} = 0) = \frac{4\pi^2 e^2 \hbar^2}{\Omega \omega^2 m_e^2} \sum_{c,v,\mathbf{k}} 2 w_{\mathbf{k}} \delta(\varepsilon_{c\mathbf{k}} - \varepsilon_{v\mathbf{k}} - \omega) \times M_\alpha^{v\to c} M_\beta^{v\to c *}, \tag{1}$$

where M and ε denote momentum matrix elements and orbital energies. Here, we consider excitations only between valence (v) and conduction (c) bands. The components of the dielectric tensor are indexed by the Cartesian indices α and β. Ω, e, and m_e denote the unit-cell volume, electron charge, and mass of the electron, respectively. In the projector augmented-wave (PAW) [46] method the all-electron orbitals $|\psi_{n\mathbf{k}}\rangle$ are given by a linear transformation of the pseudo-orbitals $|\tilde{\psi}_{n\mathbf{k}}\rangle$:

$$|\psi_{n\mathbf{k}}\rangle = |\tilde{\psi}_{n\mathbf{k}}\rangle + \sum_i (|\phi_i\rangle - |\tilde{\phi}_i\rangle)\langle \tilde{p}_i | \tilde{\psi}_{n\mathbf{k}}\rangle. \tag{2}$$

The pseudo-orbitals depend on the band index n and crystal momentum $\mathbf{k}$. $|\phi_i\rangle$, $|\tilde{\phi}_i\rangle$, and $|\tilde{p}_i\rangle$ are all-electron partial waves, pseudopartial waves, and the projectors, respectively. The index i is a shorthand for the atomic site and other indices enumerating these quantities at each site (such as angular and magnetic quantum numbers). In the PAW formalism, the matrix elements are given by

$$M_\alpha^{v\to c} = \langle \psi_{c\mathbf{k}} | i\nabla_\alpha - \mathbf{k}_\alpha | \psi_{v\mathbf{k}}\rangle = \langle \tilde{\psi}_{c\mathbf{k}} | i\nabla_\alpha - \mathbf{k}_\alpha | \tilde{\psi}_{v\mathbf{k}}\rangle + \sum_{ij} \langle \tilde{\psi}_{c\mathbf{k}} | \tilde{p}_i\rangle \langle \tilde{p}_j | \tilde{\psi}_{v\mathbf{k}}\rangle i(\langle \phi_i | \nabla_\alpha | \phi_j\rangle - \langle \tilde{\phi}_i | \nabla_\alpha | \tilde{\phi}_j\rangle), \tag{3}$$

where the one-center terms are calculated within the PAW sphere for each atom.

Since in x-ray absorption spectroscopy, one only considers one core hole at a single site, we can from now on restrict the equations to a single site. The index i then only enumerates the main quantum number, the angular and the magnetic quantum numbers. As usual in the PAW method, using the completeness relation, $\sum_i |\tilde{p}_i\rangle\langle\tilde{\phi}_i| = 1$, the first and third terms in Eq. (3) cancel each other leading to the following simplified matrix elements:

$$M_\alpha^{\text{core}\to c\mathbf{k}} = \sum_i \langle \tilde{\psi}_{c\mathbf{k}} | \tilde{p}_i\rangle \langle \phi_i | \nabla_\alpha | \phi_{\text{core}}\rangle. \tag{4}$$

Also, the summation over bands in Eq. (1) can be limited to the conduction bands c:

$$\epsilon^{(2)}_{\alpha\beta}(\omega) = \frac{4\pi^2 e^2 \hbar^2}{\Omega \omega^2 m_e^2} \sum_{c,\mathbf{k}} 2 w_{\mathbf{k}} \delta(\varepsilon_{c\mathbf{k}} - \varepsilon_{\text{core}} - \omega) \times M_\alpha^{\text{core}\to c\mathbf{k}} M_\beta^{\text{core}\to c\mathbf{k}*}. \quad (5)$$

The equations used in the full-potential augmented-plane-wave method are very similar to the ones used in the PAW method and are hence not presented here (details for the calculations of the dielectric function within the full-potential augmented-plane-wave method can be found in Ref. [47]).

III. DIELECTRIC FUNCTION WITHIN THE BSE

The diagonal part of the dielectric function using the Bethe-Salpeter equation [21–24] is given by

$$\varepsilon^{(2)}_{\alpha\alpha}(\omega) = \frac{4\pi^2 e^2 \hbar^2}{\Omega \omega^2 m_e^2} \sum_{\lambda} \left| \sum_{c,\mathbf{k}} A^{\lambda}_{\text{core},c\mathbf{k}} M_\alpha^{\text{core}\to c\mathbf{k}} \right|^2 \times \delta(\varepsilon^{\lambda} - \omega). \quad (6)$$

This equation is similar to Eq. (5) but with the difference that the electron-hole channels at different wave vectors $\mathbf{k}$ are coupled by the eigenstates of the BSE $A^{\lambda}_{\text{core},c\mathbf{k}}$ with excitation frequencies ε^{λ}, where λ labels the eigenstates. The BSE eigenstates $A^{\lambda}_{\text{core},c\mathbf{k}}$ are obtained by solving the Bethe-Salpeter equation in the Tamm-Dancoff approximation [48,49]. Details of the method for valence electrons can be found in Ref. [25]. Commonly, for K edges only a single core state ($1s$) is included as occupied state in the core-valence BSE since inclusion of other core electrons or occupied valence states usually does not change the spectrum [26].

IV. ELECTRON-PHONON COUPLINGS

The inclusion of parameter-free electron-phonon coupling (EPC) in *ab initio* calculations is mainly achieved via two approaches. The first one relies on perturbation theory to incorporate the coupling. In second order and neglecting the energy of the emitted or absorbed phonon, this leads to the often used Allen-Heine-Cardona approach [50–52]. Generally, it is not trivial to extend this method to the influence of lattice vibrations on say a spectroscopic quantity. For instance, one can not easily calculate the changes in the core to valence transition matrix elements $M^{\text{core}\to c\mathbf{k}}$. A detailed and comprehensive review of state-of-the art methods for EPC is given in Ref. [53].

The second approach is based on statistical averages over the vibrational eigenmodes of the system. These can be obtained in numerous ways, for example, by Monte Carlo integration [54,55], molecular dynamics [56,57], or path-integral molecular dynamics [58,59]. Motivated by the fact that for increasing supercell sizes, the number of required structures in the Monte Carlo method is decreasing, Giustino and coworkers [60] proposed a method where for a given temperature only a single structure is required. The displacements from the equilibrium structure are given by

$$\Delta\tau^{\text{OS}}_{\kappa} = \sqrt{\frac{1}{M_\kappa}} \sum_{\nu}^{3(N-1)} (-1)^{\nu-1} \mathbf{e}_{\kappa,\nu} \sigma_{\nu,T}, \quad (7)$$

where $\mathbf{e}_{\kappa,\nu}$ denotes the unit vector of eigenmode ν on atom κ. The summation over the eigenmodes runs in an ascending order with respect to the values of the eigenfrequencies, and the magnitude of each displacement is given by

$$\sigma_{\nu,T} = \sqrt{\left(n_{\nu,T} + \frac{1}{2}\right) \frac{\hbar}{\omega_\nu}}. \quad (8)$$

Here, $n_{\nu,T} = [\exp(\hbar\omega_\nu / k_B T) - 1]^{-1}$ denotes the Bose-Einstein occupation number. For all eigenmodes the displacements according to Eq. (7) are linearly combined and added to the equilibrium positions. The resulting single structure is then directly used in the electronic structure calculations. This means that although the phonons are calculated in the harmonic approximation, the electronic effects are calculated up to all orders available in the applied electronic structure method. This is an advantage compared to a perturbative method, where the accuracy is restricted to the order of the perturbation theory, which is usually of second order. Furthermore, the method can be easily applied to any observable, and no additional coding is required.

V. COMPUTATIONAL METHODS

The SCH method was used in our calculations. In this method, a core hole is artificially introduced on one of the atoms [61,62] and this electron is added to the valence electrons during self-consistency. The size of the supercell was tested for convergence, and we found that a cell size of $4 \times 4 \times 2$ is sufficient to obtain converged results. We employ the experimental lattice parameters of $a = 2.504$Å and $c = 6.661$Å in all calculations since, for many DFT functionals, the optimization of c, which depends on weak interactions, is problematic. If not stated otherwise, all SCH calculations were carried out using the VASP [63–65] code using the PAW method. A plane-wave cutoff of 320 eV and a k-point sampling of $5 \times 5 \times 3$ was employed in all calculations. For the description of electron exchange and correlation, the generalized gradient approximation (GGA) of Perdew, Burke, and Ernzerhof (PBE) was used [66].

To verify our results, the all-electron code WIEN2K [67], which is based on the augmented-plane-wave + local-orbitals (APW+lo) basis set, was used. In this method, the unit cell is decomposed into an interstitial region described by a plane-wave expansion and atomic spheres (with radii of 1.29 and 1.43 bohr for boron and nitrogen, respectively) described by radial wave functions multiplied by spherical harmonics. A basis-set cutoff of $RK_{max} = 7$ was used in all calculations, where R denotes the atomic radius of the smallest atomic sphere and K_{max} is the magnitude of the largest reciprocal lattice vector. The SCH calculations were carried out in analogy to the VASP calculations. Additionally to the SCH method, the WIEN2K code was also used to perform BSE calculations [26]. In the BSE method, the calculations are performed for the primitive cell, where the wave functions and eigenenergies

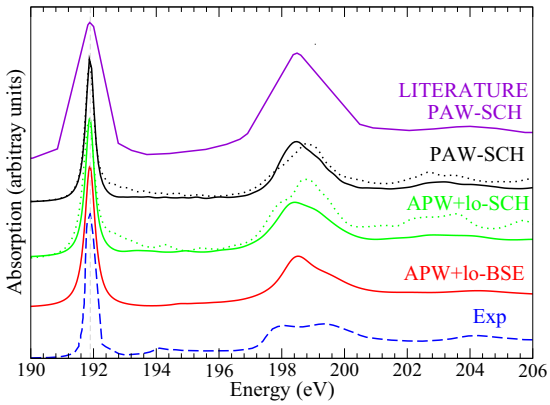

FIG. 1. The boron K-edge absorption spectra. The continuous and dotted lines represent calculations employing full- and half-core holes, respectively. The experimental spectrum was taken from Ref. [8]. The spectrum labeled as "literature PAW-SCH" was extracted from Ref. [43], where the CASTEP code was used.

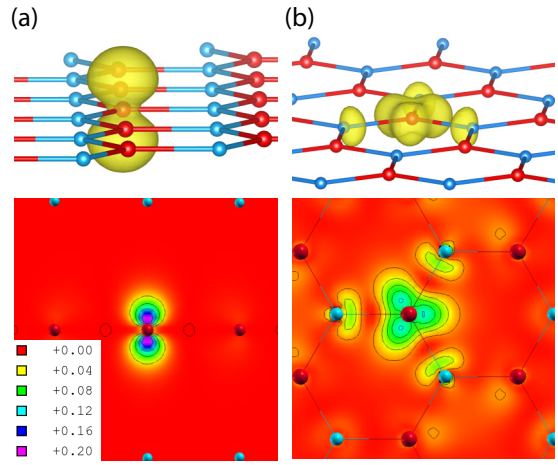

FIG. 2. Electron density for the unoccupied bands from a boron SCH calculation. (a), (b) Show the electron densities corresponding to the first and second major peaks in the spectra shown in Fig. 1, respectively. The contour plots (in electrons per bohr^3) in (a) and (b) are shown in the (110) and (001) planes, respectively. Red and blue spheres indicate boron and nitrogen, respectively.

obtained from the DFT calculations are used as starting point for the BSE calculations. The convergence of the results with respect to the number of considered conduction bands and the k mesh was tested in all calculations, and k meshes of $14 \times 14 \times 4$ were used. The cutoffs for the maximal reciprocal lattice vector G_{max} in the calculations of the dielectric matrix, the direct term of the BSE Hamiltonian, and the exchange term were tested carefully for convergence and G_{max} of 6, 4, and 6 bohr^{-1} were used for these three terms, respectively.

All calculated absorption spectra for the boron K edge were scaled to reproduce the height of the first peak and broadened such that the first main peak gives the same width at half-maximum. The nitrogen K-edge spectrum was processed analogously but with the second main peak as reference. All theoretical spectra were broadened with a Lorentzian function employing a linearly energy-dependent broadening parameter $\sigma(E) = \sigma_0 + (E - \theta)k$, where θ describes an offset for the energy dependence of the broadening function. Below this value, the broadening parameter σ_0 is constant. Parameter sets of $\sigma_0 = 0.3$ and 0.5 eV, $\theta = 192$ and 394 eV, and $k = 0.04$ and 0.3 were employed for boron and nitrogen, respectively. For nitrogen, the experimental broadening is larger than for boron because of the higher binding energies.

VI. SPECTRA FOR GROUND-STATE STRUCTURES

In this section, we evaluate the calculated XANES spectra for the equilibrium ground-state structure without considering vibrational displacements.

A. Boron K edge

Figure 1 shows the calculated absorption spectra of the boron K edge in various approximations and compares them with experiment. The theoretical spectra are aligned such that the first peak ($2p_{\pi^*}$, in the following simply π^*) matches the experimental position. The experimental spectrum shows four features: a strong resonance at 192 eV, a double peak at 199 eV, and two weak structures at 194 and 204 eV, respectively. In the following, we will discuss these peaks in detail.

Obviously, both, SCH and BSE calculations find a very narrow first peak in agreement with experiment. It originates from a single exciton in BSE, while in the SCH calculations it stems from a very narrow (almost dispersionless) band at the onset of the conduction bands, which we do not show here explicitly. This peak is entirely described by excitations into states perpendicular to the hexagonal BN layers and the corresponding electron density is plotted in Fig. 2(a). The distinct p_z character (orthogonal to the hexagonal plane) of this state is clearly visible, and the electron density of this resonance is localized on the atom containing the core hole.

From the excitonic contributions, shown in Fig. 3(a), it can be also seen that only contributions in z direction are involved in the first peak. The strong localization, in fact, leads to a single excitonic contribution with a binding energy of 4.44 eV [see Figs. 3(a) and 3(c)]. This energy is clearly higher than the previously reported energies of 1.7–1.9 eV from Refs. [68,69]. The definition of the binding energy (see caption of Fig. 3) might differ from literature, where the independent particle results are compared with BSE.

The small peak at 194.1 eV in the experimental spectrum of Ref. [8] seems to correspond to the onset of many electron-hole pairs in the BSE calculations. In the calculations, these excitations have only very little oscillator strength and are, therefore, hardly visible in the final BSE spectrum. It is conceivable that finite-temperature effects increase the oscillator strength since displacements will lower the symmetry and make previously quiet transitions optically active.

The experimental $2p_{\sigma^*}$ resonance (from now only simply σ^*) is measured as a broad double peak centered at approximately 199 eV in Ref. [8]. As noted before [43], our SCH calculations give instead of the double peak only a single peak. Also, the separation between this peak and the first peak is slightly smaller than in experiment. The BSE calculations show no improvement compared to the SCH calculation and give practically the same result. From Fig. 3(b) we can see that

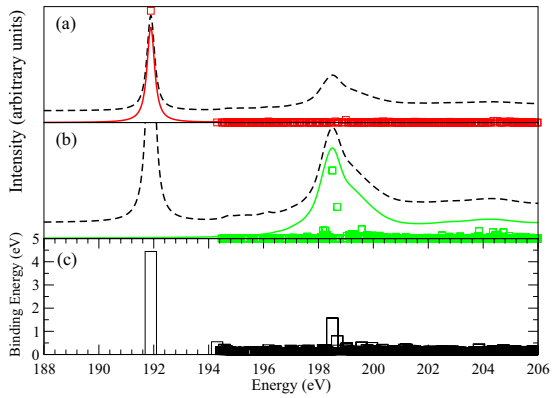

FIG. 3. Contributions to the boron K-edge absorption spectrum using BSE. Black broken line shows the total spectrum. Red lines in (a) and green lines in (b) correspond to contributions of p_z and $p_{x/y}$ character, respectively. The oscillator strength of individual excitons is marked by squares. The black dashed line corresponds to the total BSE spectrum. (c) Shows the binding energy of the individual excitons. This was calculated as the average difference between the quasiparticle energies and the excitation energy $\varepsilon^{\lambda}_{\text{bind}} = \sum_{c\mathbf{k}} |A^{\lambda}_{\text{core},c\mathbf{k}}|^2(\varepsilon_{c\mathbf{k}} - \varepsilon_{\text{core}}) - \varepsilon^{\lambda}$.

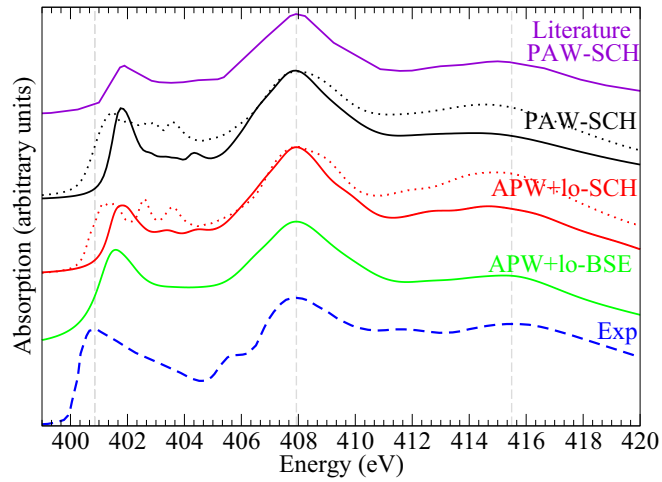

FIG. 4. The nitrogen K-edge absorption spectra. The continuous and dotted lines represent calculations employing full- and half-core holes, respectively. The experimental spectrum was taken from Ref. [12]. The spectrum labeled as "literature PAW-SCH" was extracted from Ref. [43] and the CASTEP code was used to obtain it.

several excitons with mainly p_x and p_y character contribute to the spectrum with different oscillator strength. Their binding energies are much smaller than for the main π^* resonance, and vary from 0–1.5 eV [Fig. 3(c)]. In the SCH calculations, the states responsible for this spectral feature are not so well separated from other states, but we can still plot their electron densities as shown in Fig. 2(b). The density originates from $p_{x/y}$ states on the boron atom. The states are not as well localized as the corresponding p_z counterpart and there is a significant antibonding interaction with the neighboring nitrogen atoms. This is evidenced by the node between the atoms and the asphericity towards the center of the hexagons. This peak in the spectrum can thus indeed be classified as originating from σ^* states.

Last but not least, there is a small peak slightly above 204 eV in the experimental spectrum. This is nicely reproduced in BSE but mispositioned by about 1 eV in the SCH calculations. This is essentially the only feature where BSE yields an improvement over DFT SCH calculations.

B. Nitrogen K edge

The calculated absorption spectra together with the experimental spectrum for the nitrogen K edge are shown in Fig. 4. The theoretical spectra are shifted such that the second peak is aligned both in position and intensity to the experimental data. Altogether, the experimental spectrum is well reproduced by all methods with a few features that we will discuss in the following.

Starting with the third peak, we observe that BSE gives a slight improvement over SCH calculations. The latter are shifted to smaller energies by approximately 0.5 eV compared to the experimental peak maximum (at 415.5 eV). From Figs. 5(b) and 5(c), one can conclude that this broad peak consists of many excitons with binding energies of less than 0.5 eV in the hexagonal BN plane (xy plane) and very small contributions in the z direction.

For the second peak, all calculational methods yield a broad peak with main contributions in the xy plane. A small bump on the left shoulder of the experimental spectrum at 405.5 eV is clearly visible. The SCH calculations do not show this peak. The BSE gives an excitonic state at that position, as can be seen from Fig. 5. However, the overall intensity in the spectrum is too small compared to the experiment.

Figure 6(b) shows the electron density corresponding to a 0.5-eV energy window around the second peak. It can be

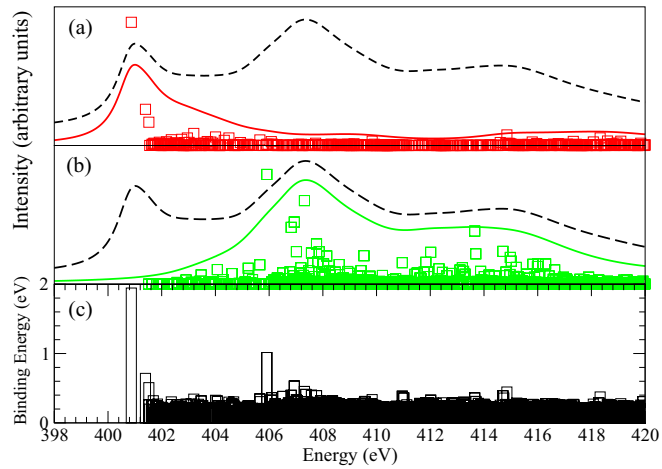

FIG. 5. Contributions to the nitrogen K-edge absorption spectrum obtained using BSE. Red lines in (a) and green lines in (b) correspond to contributions in the z and xy planes, respectively. The same color scheme applies to the excitons represented as squares. The black dashed line corresponds to the whole BSE spectrum. (c) Shows the binding energy of the excitons. This was calculated as the average difference between the quasiparticle energies and the excitation energy $\varepsilon^{\lambda}_{\text{bind}} = \sum_{c\mathbf{k}} |A^{\lambda}_{\text{core},c\mathbf{k}}|^2(\varepsilon_{c\mathbf{k}} - \varepsilon_{\text{core}}) - \varepsilon^{\lambda}$.

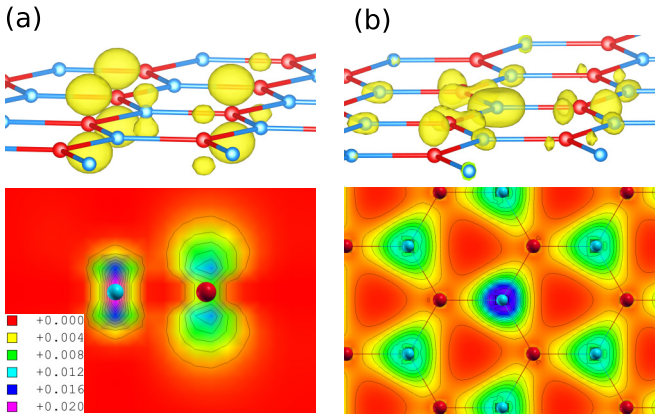

FIG. 6. Electron density for the unoccupied bands within the SCH calculation for the nitrogen K edge. (a), (b) Show the electron density for the first and second peaks of the corresponding spectrum in Fig. 5, respectively. The contour-line plot in (a) shows the nitrogen with the core hole and one next-neighbor boron atom. The y axis points towards the z direction within the crystal. The contour-line plot in (b) shows the electron density within the (001) plane (units in electrons per bohr^3). Red and blue spheres indicate boron and nitrogen, respectively.

seen that the largest contributions to the electron density are on the central atom with the core hole. Nevertheless, the states are quite delocalized in space since there are significant contributions on the next-neighbor nitrogen atoms in the xy plane. This also explains the strong broadening of the second peak.

We now turn to the first peak in the spectrum. Figure 7 shows the DOS for (a) a nitrogen atom with a core hole, (b) one of its next-neighbor boron atoms, and (c) a nitrogen atom without a core hole. All three atoms show peaks with p_z character at the onset of the conduction bands, but the intensity of the peak is largest on the nearest-neighbor boron

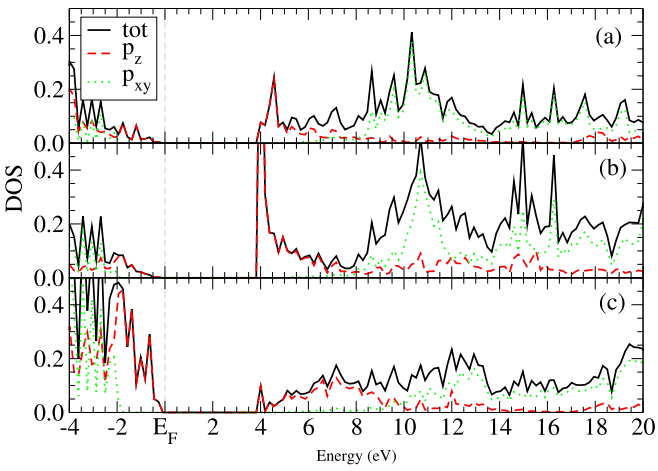

FIG. 7. Partial densities of states for the SCH calculations employing a core hole on nitrogen for different atoms. The nitrogen atom with the core hole is shown in (a). The next-neighbor boron and nitrogen atoms in the hexagonal plane are shown in (b) and (c), respectively. The units for the densities of states are in number of states per eV.

atoms and not the central nitrogen atom with the hole. This exciton is thus fairly delocalized. The overall p_z-like character of the first peak can be also clearly seen from the electron density plots in Fig. 6(a).

Concerning the energetic position of this peak, we observe fairly large discrepancies compared to experiment. Compared to the central peak (at 408 eV), the first peak is generally at too high binding energies in all SCH calculations (about 402 eV instead of 401 eV). Using the BSE, the position of this peak is only slightly improved. A strong k-mesh dependency is ruled out as reason for the deviation of the BSE results compared to experiment since we have very carefully investigated the convergence of the spectra with respect to the k mesh. The k-mesh convergence for the nitrogen K edge is even faster than for the boron K edge, and the k mesh of $14 \times 14 \times 4$ yields fully converged results. We have also tested the local density approximation [70] within the SCH method and the results are very similar to PBE. Therefore, the reason for the difference between the experiment and theory remains unclear, but is probably related to the quite delocalized nature of the exciton and errors in the single-particle energy of nitrogen and boron p states. A sizable change of the spectrum is only observed, if in the SCH spectrum only half an electron is moved from the core to the valence (see dotted lines in Fig. 4). This approach is sometimes used in literature and is inspired by Slater's transition state method. This result might indicate that the final-state (sudden) approximation, which assumes that all electrons act instantaneously to the excitation of the core electron, is not valid for the nitrogen K edge. From a quantitative point of view, however, this method also does not yield satisfactory results.

VII. SPECTRA INCLUDING ZERO-POINT VIBRATIONS

The spectra including zero-point vibrations and finite-temperature structures are calculated along the following lines. First, the vibrational modes of the ground-state structure are determined. Then, a single representative structure at a specific temperature (in our case at $T = 0$, since we include only zero-point vibrations) is obtained according to Eq. (7). Finally, SCH calculations are carried out for each ion of one specific type in the supercell, as the environment of each atom is different as a result of the deformations. The spectra are obtained as an average of the individual spectra obtained for all atoms of one species. For the $4 \times 4 \times 2$ cell, we sum over 64 atoms in the unit cell for both boron and nitrogen.

Spectra for the boron K edge with and without considering zero-point vibrations are shown in Fig. 8. It can be clearly seen that the structure of the double peak in the experimental spectrum is only reproduced by including zero-point vibrations. The origin of the splitting can be traced back to a symmetry reduction of the environment of the boron atom with the core hole, as shown in Fig. 9. The charge density of the undistorted structure given in Fig. 9(a) is symmetric with respect to the next-neighbor nitrogen atoms in the hexagonal plane. This means that the p_x and p_y orbitals are energetically degenerate resulting in a single peak in the p DOS (shown in the lower part of Fig. 10). The small peak at approximately 9 eV (which is at the onset of the σ^* peak) in the total DOS of the single-boron atom has almost purely s character and

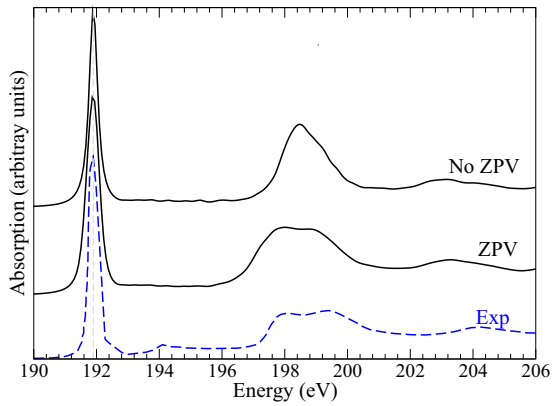

FIG. 8. Boron K-edge spectra including zero-point vibrations (ZPV) and without zero-point vibrations (no ZPV). The experimental spectrum was taken from Ref. [8].

is not of any relevance for the spectrum since a transition of a boron 1s state into this state is optically forbidden. By including zero-point vibrations, the instantaneous positions of all atoms are moved out of the high-symmetry position.

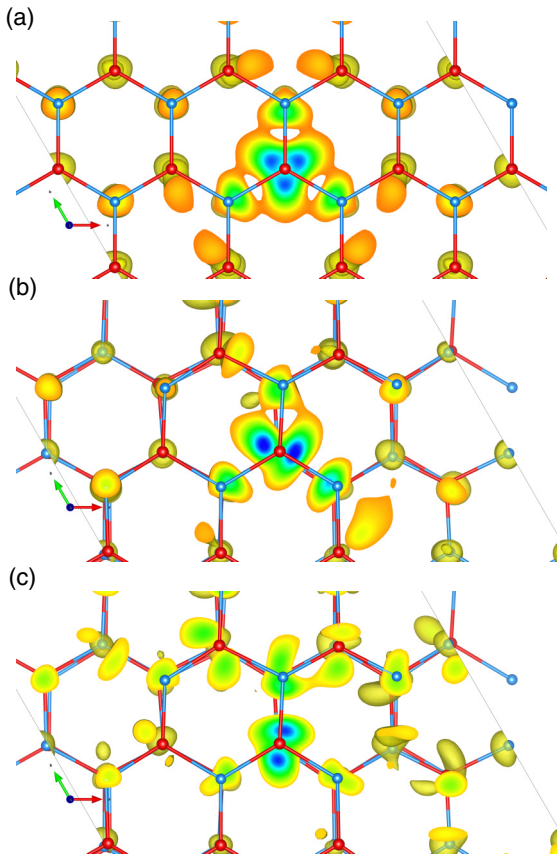

FIG. 9. Electron densities corresponding to an energy window of about 1.5 eV around the center of the boron π^* peak for a boron atom with a core hole. (a) Shows the results for the undistorted structure. (b), (c) Show the results for one boron atom for the first and second shoulders (yellow and red area highlighting in Fig. 10), respectively, and including zero-temperature displacements. Red and blue spheres indicate boron and nitrogen, respectively.

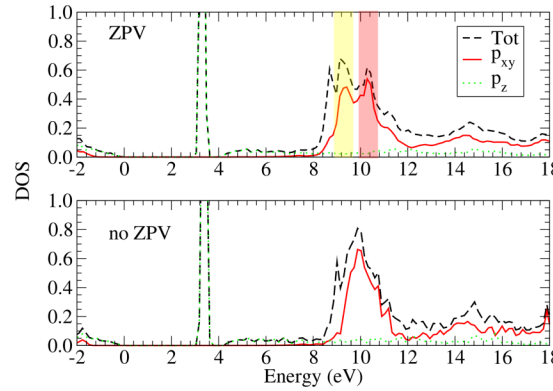

FIG. 10. DOS and partial DOS for a boron atom with a core hole including zero-point vibrations (ZPV) and without zero-point vibrations (no ZPV).

Inferential, each boron atom now has one nitrogen neighbor with a shorter boron-nitrogen bond as well as two neighbors with longer boron-nitrogen bonds. This leads to the formation of two distinct p_x and p_y hybrid orbitals, let us call them $p_\parallel$ and p_{norm}, one being parallel to the short boron-nitrogen bond, and the other one being orthogonal to the short boron-nitrogen bond. The one parallel to the short boron-nitrogen bond is pushed up in energy since it experiences strong Pauli repulsion from the occupied neighboring nitrogen p orbital, causing the upper shoulder (red area in Fig. 10), whereas the other one is found at lower binding energies (yellow area in Fig. 10). The remarkable observation is that the splitting prevails even when averaged over the local environment of many boron atoms.

Figure 11 shows the boron K-edge spectrum at different temperatures. The spectra were scaled, such that the height of the first peak remains identical. The height difference between the first two peaks becomes minimally smaller and the double peak gets broader with increasing temperature. Besides, the spectra are very similar to each other, and hence we deduce that the zero-point motions are the main reason for the double-peak structure of the σ^* peak.

Similarly as for boron, we have tested the effect of zero-point vibrations for nitrogen, yielding the spectrum plotted in Fig. 12. In contrast to boron, no significant further broadening

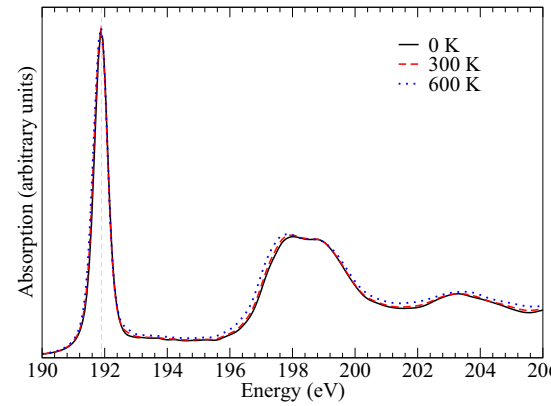

FIG. 11. Temperature dependence of the boron K-edge spectra.

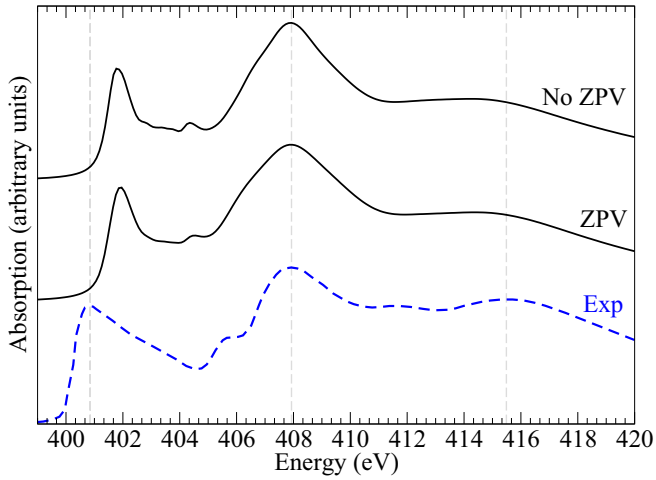

FIG. 12. Nitrogen K-edge spectra including zero-point vibrations (ZPV) and without zero-point vibrations (no ZPV). The experimental spectrum was taken from Ref. [12].

or splitting due to symmetry breaking is visible for any peak and the results including zero-point vibrations are practically the same as for the ground-state calculations. Only the peaks are slightly broadened as a result of thermal vibrations.

VIII. CONCLUSION

In this paper, we have conducted state-of-the-art calculations to determined the XANES spectra of the boron and nitrogen K edge in h-BN. Specifically, we have employed the supercell core-hole (SCH) and the BSE approaches. To compare with previous studies, we have first performed the calculations at the equilibrium ionic structures. Overall, we find excellent agreement between PAW and APW+lo calculations for SCH calculations. However, both as well as all previous studies show important discrepancies to experiment prompting us to apply the BSE approach, which accounts for important many-body effects that are absent in the present density functionals [32–34]. Unfortunately for h-BN, the BSE shows no noteworthy improvements over the SCH approach. Only small details of the spectra, such as the high-energy peak at 204 eV for boron, are slightly improved. This means that some experimental features remain unexplained employing the ionic ground-state structure. As discussed below, these discrepancies can be partly remedied by including zero-point vibrations in the structure.

The important differences between experiment and theory are the position of the first and second peaks in the nitrogen spectrum, and the shape of the second peak in the boron spectrum. Specifically, the energy difference between the first (π^*) and second (σ^*) peaks in the nitrogen spectrum is too small compared to experiment, and the shape of the first peak of the nitrogen K edge is not well reproduced. In this case, inclusion of zero-point vibrations does not change the spectrum significantly. We found that the only way to improve the spectrum is to perform the calculations using half a core hole. Such calculations are sometimes used in literature, but we feel that this is a rather pedestrian and *ad hoc* solution. Nevertheless, these calculations indicate that something is possibly amiss in the description of the screening of the core hole by the π^* orbitals. This could imply that the sudden approximation is not accurate enough, which might well be as the excitonic π^* state is found to be quite delocalized in our calculations. Alternatively, DFT, which is used in the SCH and as a starting point for the BSE calculations, might not be sufficiently accurate.

The second important difference between theory and experiment is the shape of the second peak (σ^*) in the boron spectrum. While the experiments yield a double peak with almost equal height for both subpeaks, our and all previous calculations employing the equilibrium ionic structure yield a single peak. By including zero-point vibrations in the SCH calculations, the double peak observed experimentally is very well reproduced. Obviously, the shortcoming of the undistorted ground-state calculations is that all boron atoms are in a fully symmetric position. When zero-point vibrations are included, the atoms are shifted out of their high-symmetry position. For the majority of the boron atoms, this results in an environment where one bond out of three boron-nitrogen bonds is shorter than the other two. The corresponding antibonding boron $2p_{\sigma^*}$ orbital shifts upwards, whereas the other $2p_{\sigma^*}$ orbital shifts downwards to lower binding energies, resulting in two distinct $2p_{\sigma^*}$ peaks. To the best of our knowledge, such an important qualitative effect on theoretical XANES spectra is yet unprecedented, and clearly highlights that vibrational effects can be exceedingly important for the interpretation of XANES spectra. The presented methodology to include vibrational effects is fairly easy to use. Essentially, it requires a calculation of all phonon modes in a supercell, and creation of one representative structure corresponding to the selected temperature. Only the actual SCH calculations are more involved and expensive than for the ionic ground state since one needs to average over core-hole calculations for every boron (or nitrogen) atom in the supercell since after displacement the local environment of all boron and nitrogen atoms is different. Therefore, one SCH calculation needs to be performed for every atom in the supercell. In practice, such calculations are, however, quite straightforward and efficient. This paves the way towards routine calculations of XANES spectra including zero-point vibrations or even finite-temperature effects. Finally, we would like to add that the above methodology is not limited to core-electron spectroscopy and in principle it can be included in the calculation of any other observable. Examples for other observables can be found in the original work by Giustino, where they calculated the optical absorption spectrum in the visible and UV region.

ACKNOWLEDGMENTS

E.F.-L. would like to thank the Norwegian Research Council of Norway (Project No. 262339) and SINTEF for providing financial support for this work. G.K. and P.B. acknowledge support by the project F41 (SFB ViCoM) of the Austrian Science Fund (FWF).

[1] K. Watanabe, T. Taniguchi, and H. Kanda, Nat. Mater. **3**, 404 (2004).

[2] C. Dean, A. Young, I. Meric, C. Lee, L. Wang, S. Sorgenfrei, K. Watanabe, T. Taniguchi, P. Kim, K. Shepard *et al.*, Nat. Nanotechnol. **5**, 722 (2010).

[3] E. Tegeler, N. Kosuch, G. Wiech, and A. Faessler, Phys. Status Solidi B **91**, 223 (1979).

[4] A. Mansour and S. E. Schnatterly, Phys. Rev. B **36**, 9234 (1987).

[5] J. Moscovici, G. Loupias, P. Parent, and G. Tourillon, J. Phys. Chem. Solids **57**, 1159 (1996).

[6] J. J. Jia, T. A. Callcott, E. L. Shirley, J. A. Carlisle, L. J.Terminello, A. Asfaw, D. L. Ederer, F. J. Himpsel, and R. C. C. Perera, Phys. Rev. Lett. **76**, 4054 (1996).

[7] R. Gago, I. Jimenez, J. Albella, and L. Terminello, Appl. Phys. Lett. **78**, 3430 (2001).

[8] L. Hua Li, M. Petravic, B. Cowie, T. Xing, R. Peter, Y. Chen, C. Si, and W. Duan, Appl. Phys. Lett. **101**, 191604 (2012).

[9] R. Franke, S. Bender, J. Hormes, A. Pavlychev, and N. Fominych, Chem. Phys. **216**, 243 (1997).

[10] A. B. Preobrajenski, A. S. Vinogradov, M. L. Ng, E. Ćavar, R. Westerström, A. Mikkelsen, E. Lundgren, and N. Mårtensson, Phys. Rev. B **75**, 245412 (2007).

[11] P. Moreau, F. Boucher, G. Goglio, D. Foy, V. Mauchamp, and G. Ouvrard, Phys. Rev. B **73**, 195111 (2006).

[12] M. Petravic, R. Peter, M. Varasanec, L. Li, Y. Chen, and B. Cowie, J. Vac. Sci. Technol. A **31**, 031405 (2013).

[13] K. Lawniczak-Jablonska, T. Suski, I. Gorczyca, N. E. Christensen, K. E. Attenkofer, R. C. C. Perera, E. M. Gullikson, J. H. Underwood, D. L. Ederer, and Z. LilientalWeber, Phys. Rev. B **61**, 16623 (2000).

[14] H. Choi, S. Bae, W. Jang, J. Park, H. Song, and H.-J. Shin, J. Phys. Chem. B **109**, 7007 (2005).

[15] R. Peter, A. Bozanic, M. Petravic, Y. Chen, L.-J. Fan, and Y.-W. Yang, J. Appl. Phys. **106**, 083523 (2009).

[16] J. Rehr, J. Kas, F. Vila, M. Prange, and K. Jorissen, Phys. Chem. Chem. Phys. **12**, 5503 (2010).

[17] A. Paxton, M. van Schilfgaarde, M. MacKenzie, and A. Craven, J. Phys.: Condens. Matter **12**, 729 (2000).

[18] J. Luitz, M. Maier, C. Hébert, P. Schattschneider, P. Blaha, K. Schwarz, and B. Jouffrey, Eur. Phys. J. B **21**, 363 (2001).

[19] C. J. Pickard and M. C. Payne, *Ab initio EELS: Beyond the Fingerprint*, Vol. 153 (Institute of Physics Publishing, Bristol, 1997).

[20] D. N. Jayawardane, C. J. Pickard, L. M. Brown, and M. C. Payne, Phys. Rev. B **64**, 115107 (2001)

[21] E. Salpeter and H. Bethe, Phys. Rev. **84**, 1232 (1951).

[22] G. Strinati, Phys. Rev. Lett. **49**, 1519 (1982).

[23] G. Strinati, Phys. Rev. B **29**, 5718 (1984).

[24] G. Strinati, Riv. Nuovo Cimento Ser. 3 **11**, 1 (1988).

[25] M. Rohlfing and S. G. Louie, Phys. Rev. B **62**, 4927 (2000).

[26] R. Laskowski and P. Blaha, Phys. Rev. B **82**, 205104 (2010).

[27] F. Karsai, P. Tiwald, R. Laskowski, F. Tran, D. Koller, S. Gräfe, J. Burgdörfer, L. Wirtz, and P. Blaha, Phys. Rev. B **89**, 125429 (2014).

[28] P. Tiwald, F. Karsai, R. Laskowski, S. Gräfe, P. Blaha, J. Burgdörfer, and L. Wirtz, Phys. Rev. B **92**, 144107 (2015).

[29] T. Galvani, F. Paleari, H. P. C. Miranda, A. Molina-Sńchez, L. Wirtz, S. Latil, H. Amara, and F. Ducastelle, Phys. Rev. B **94**, 125303 (2016).

[30] C.-H. Park, C. D. Spataru, and S. G. Louie, Phys. Rev. Lett. **96**, 126105 (2006).

[31] A. L. Ankudinov, Y. Takimoto, and J. J. Rehr, Phys. Rev. B **71**, 165110 (2005).

[32] W. Olovsson, I. Tanaka, P. Puschnig, and C. Ambrosch-Draxl, J. Phys.: Condens. Matter **21**, 104205 (2009).

[33] W. Olovsson, I. Tanaka, T. Mizoguchi, P. Puschnig, and C. Ambrosch-Draxl, Phys. Rev. B **79**, 041102 (2009).

[34] W. Olovsson, I. Tanaka, T. Mizoguchi, G. Radtke, P. Puschnig, and C. Ambrosch-Draxl, Phys. Rev. B **83**, 195206 (2011).

[35] W. Olovsson, L. Weinhardt, O. Fuchs, I. Tanaka, P. Puschnig, E. Umbach, C. Heske, and C. Draxl, J. Phys.: Condens. Matter **25**, 315501 (2013).

[36] K. Tomita, T. Miyata, W. Olovsson, and T. Mizoguchi, J. Phys. Chem. C **120**, 9036 (2016).

[37] J. A. Carlisle, E. L. Shirley, L. J. Terminello, J. J. Jia, T. A. Callcott, D. L. Ederer, R. C. C. Perera, and F. J. Himpsel, Phys. Rev. B **59**, 7433 (1999).

[38] E. L. Shirley, Phys. Rev. Lett. **80**, 794 (1998).

[39] Y. Feng, J. A. Soininen, A. L. Ankudinov, J. O. Cross, G. T. Seidler, A. T. Macrander, J. J. Rehr, and E. L. Shirley, Phys. Rev. B **77**, 165202 (2008).

[40] E. Shirley, J. Electron Spectrosc. Relat. Phenom. **110**, 305 (2000).

[41] R. Laskowski, T. Gallauner, P. Blaha, and K. Schwarz, J. Phys.: Condens. Matter **21**, 104210 (2009).

[42] M. Jaouen, G. Hug, B. Ravel, A. Ankudinov, and J. Rehr, Europhys. Lett. **49**, 343 (2000).

[43] N. McDougall, R. Nicholls, J. Partridge, and D. McCulloch, Microsc. Microanal. **20**, 1053 (2014).

[44] J. Meyer, A. Chuvilin, G. Algara-Siller, J. Biskupek, and U. Kaiser, Nano Lett. **9**, 2683 (2009).

[45] R. Nemausat, C. Gervais, C. Brouder, N. Trcera, A. Bordage, C. Coelho-Diogo, P. Florian, A. Rakhmatullin, I. Errea, L. Paulatto *et al.*, Phys. Chem. Chem. Phys. **19**, 6246 (2017).

[46] P. E. Blöchl, Phys. Rev. B **50**, 17953 (1994).

[47] C. Ambrosch-Draxl and J. Sofo, Comput. Phys. Commun. **175**, 1 (2006).

[48] A. L. Fetter and J. D. Walecka, *Quantum Theory of Many-particle Systems* (McGraw-Hill, New York, 1971).

[49] J.-W. Van der Horst, P. A. Bobbert, M. A. J. Michels, G. Brocks, and P. J. Kelly, Phys. Rev. Lett. **83**, 4413 (1999).

[50] B. Chakraborty and P. Allen, J. Phys. C: Solid State Phys. **11**, L9 (1977).

[51] P. B. Allen and M. Cardona, Phys. Rev. B **23**, 1495 (1981).

[52] P. B. Allen and M. Cardona, Phys. Rev. B **27**, 4760 (1983).

[53] F. Giustino, Rev. Mod. Phys. **89**, 015003 (2017).

[54] B. Monserrat, N. D. Drummond, C. J. Pickard, and R. J. Needs, Phys. Rev. Lett. **112**, 055504 (2014).

[55] C. Patrick and F. Giustino, Nat. Commun. **4**, 2006 (2013).

[56] J. Lahnsteiner, G. Kresse, A. Kumar, D. D. Sarma, C. Franchini, and M. Bokdam, Phys. Rev. B **94**, 214114 (2016).

[57] D. Pan, Q. Wan, and G. Galli, Nat. Commun. **5**, 3919 (2014).

[58] R. Ramírez, C. P. Herrero, and E. R. Hernández, Phys. Rev. B **73**, 245202 (2006).

[59] M. A. Morales, J. M. McMahon, C. Pierleoni, and D. M. Ceperley, Phys. Rev. B **87**, 184107 (2013).

[60] M. Zacharias and F. Giustino, Phys. Rev. B **94**, 075125 (2016).

[61] I. Tanaka and T. Mizoguchi, J. Phys.: Condens. Matter **21**, 104201 (2009).
[62] I. Tanaka, T. Mizoguchi, and T. Yamamoto, J. Am. Ceram. Soc. **88**, 2013 (2005).
[63] G. Kresse and J. Hafner, Phys. Rev. B **47**, 558 (1993).
[64] G. Kresse and J. Furthmüller, Phys. Rev. B **54**, 11169 (1996).
[65] G. Kresse and J. Furthmüller, Comput. Mater. Sci. **6**, 15 (1996).
[66] J. P. Perdew, K. Burke, and M. Ernzerhof, Phys. Rev. Lett. **77**, 3865 (1996).
[67] P. Blaha, K. Schwarz, G. Madsen, D. Kvasnicka, J. Luitz, R. Laskowski, F. Tran, and L. Marks, *WIEN2K: An Augmented Plane Wave plus Local Orbitals Program for Calculating Crystal Properties* (Vienna University of Technology, Austria, 2018).
[68] H. Ma, S. Lin, R. Carpenter, P. Rice, and O. Sankey, J. Appl. Phys. **73**, 7422 (1993).
[69] B. M. Davies, F. Bassani, F. C. Brown, and C. G. Olson, Phys. Rev. B **24**, 3537 (1981).
[70] J. P. Perdew and Y. Wang, Phys. Rev. B **45**, 13244 (1992).